

# Slant-gap plasmonic nanoantennas for optical chirality engineering and circular dichroism enhancement

Daniel Lin<sup>1</sup> and Jer-Shing Huang<sup>1,2,3,\*</sup>

<sup>1</sup>Department of Chemistry, National Tsing Hua University, Hsinchu 30013, Taiwan

<sup>2</sup>Center for Nanotechnology, Materials Science, and Microsystems, National Tsing Hua University, Hsinchu 30013, Taiwan

<sup>3</sup>Frontier Research Center on Fundamental and Applied Sciences of Matters, National Tsing Hua University, Hsinchu 30013, Taiwan

\*jshuang@mx.nthu.edu.tw

**Abstract:** We present a new design of plasmonic nanoantenna with slant gap for optical chirality engineering. At resonance, the slant gap provides highly enhanced electric field parallel to external magnetic field with a phase delay of  $\pi/2$ , resulting in enhanced optical chirality. We show by numerical simulations that upon linearly polarized excitation our nanoantenna can generate near field with enhanced optical chirality which can be tuned by the slant angle and resonance condition. Our design allows chiral analysis with linearly polarized light and may find applications in circular dichroism analysis of chiral matter at surface.

©2014 Optical Society of America

**OCIS codes:** (170.4520) Optical confinement and manipulation; (240.6680) Surface plasmons; (250.5403) Plasmonics; (260.6970) Total internal reflection; (310.6628) Subwavelength structures, nanostructures.

---

## References and links

1. N. J. Greenfield, "Applications of circular dichroism in protein and peptide analysis," *Trends Analyt. Chem.* **18**(4), 236–244 (1999).
2. N. Yang, Y. Tang, and A. E. Cohen, "Spectroscopy in sculpted fields," *Nano Today* **4**(3), 269–279 (2009).
3. N. Yang and A. E. Cohen, "Local geometry of electromagnetic fields and its role in molecular multipole transitions," *J. Phys. Chem. B* **115**(18), 5304–5311 (2011).
4. L. D. Barron, *Molecular Light Scattering and Optical Activity*, 2nd ed. (Cambridge University, 2004).
5. E. Hendry, R. V. Mikhaylovskiy, L. D. Barron, M. Kadodwala, and T. J. Davis, "Chiral electromagnetic fields generated by arrays of nanoslits," *Nano Lett.* **12**(7), 3640–3644 (2012).
6. M. Schäferling, X. Yin, and H. Giessen, "Formation of chiral fields in a symmetric environment," *Opt. Express* **20**(24), 26326–26336 (2012).
7. M. Meinzer, E. Hendry, and W. L. Barnes, "Probing the chiral nature of electromagnetic fields surrounding plasmonic nanostructures," *Phys. Rev. B* **88**(4), 041407 (2013).
8. Y. Tang and A. E. Cohen, "Optical chirality and its interaction with matter," *Phys. Rev. Lett.* **104**(16), 163901 (2010).
9. D. M. Lipkin, "Existence of a new conservation law in electromagnetic theory," *J. Math. Phys.* **5**(5), 696–700 (1964).
10. Y. Tang and A. E. Cohen, "Enhanced enantioselectivity in excitation of chiral molecules by superchiral light," *Science* **332**(6027), 333–336 (2011).
11. P. J. Schuck, D. P. Fromm, A. Sundaramurthy, G. S. Kino, and W. E. Moerner, "Improving the mismatch between light and nanoscale objects with gold bowtie nanoantennas," *Phys. Rev. Lett.* **94**(1), 017402 (2005).
12. L. Novotny and N. Van Hulst, "Antennas for light," *Nat. Photonics* **5**(2), 83–90 (2011).
13. P. Biagioni, J.-S. Huang, and B. Hecht, "Nanoantennas for visible and infrared radiation," *Rep. Prog. Phys.* **75**(2), 024402 (2012).
14. A. Papakostas, A. Potts, D. M. Bagnall, S. L. Prosvirnin, H. J. Coles, and N. I. Zheludev, "Optical manifestations of planar chirality," *Phys. Rev. Lett.* **90**(10), 107404 (2003).
15. M. Kuwata-Gonokami, N. Saito, Y. Ino, M. Kauranen, K. Jefimovs, T. Vallius, J. Turunen, and Y. Svirko, "Giant optical activity in quasi-two-dimensional planar nanostructures," *Phys. Rev. Lett.* **95**(22), 227401 (2005).
16. P. Biagioni, J.-S. Huang, L. Duò, M. Finazzi, and B. Hecht, "Cross resonant optical antenna," *Phys. Rev. Lett.* **102**(25), 256801 (2009).

17. P. Biagioni, M. Savoini, J.-S. Huang, L. Duò, M. Finazzi, and B. Hecht, "Near-field polarization shaping by a near-resonant plasmonic cross antenna," *Phys. Rev. B* **80**(15), 153409 (2009).
18. J. K. Gansel, M. Thiel, M. S. Rill, M. Decker, K. Bade, V. Saile, G. von Freymann, S. Linden, and M. Wegener, "Gold helix photonic metamaterial as broadband circular polarizer," *Science* **325**(5947), 1513–1515 (2009).
19. M. Decker, R. Zhao, C. M. Soukoulis, S. Linden, and M. Wegener, "Twisted split-ring-resonator photonic metamaterial with huge optical activity," *Opt. Lett.* **35**(10), 1593–1595 (2010).
20. R. Quidant and M. Kreuzer, "Biosensing: Plasmons offer a helping hand," *Nat. Nanotechnol.* **5**(11), 762–763 (2010).
21. E. Hendry, T. Carpy, J. Johnston, M. Popland, R. V. Mikhaylovskiy, A. J. Laphorn, S. M. Kelly, L. D. Barron, N. Gadegaard, and M. Kadodwala, "Ultrasensitive detection and characterization of biomolecules using superchiral fields," *Nat. Nanotechnol.* **5**(11), 783–787 (2010).
22. M. Schäferling, D. Dregely, M. Hentschel, and H. Giessen, "Tailoring enhanced optical chirality: design principles for chiral plasmonic nanostructures," *Phys. Rev.* **2**, 031010 (2012).
23. Y. Zhao, M. A. Belkin, and A. Alù, "Twisted optical metamaterials for planarized ultrathin broadband circular polarizers," *Nat Commun* **3**, 870 (2012).
24. X. B. Shen, A. Asenjo-Garcia, Q. Liu, Q. Jiang, F. J. García de Abajo, N. Liu, and B. Q. Ding, "Three-dimensional plasmonic chiral tetramers assembled by DNA origami," *Nano Lett.* **13**(5), 2128–2133 (2013).
25. V. K. Valev, J. J. Baumberg, C. Sibilia, and T. Verbiest, "Chirality and chiroptical effects in plasmonic nanostructures: fundamentals, recent progress, and outlook," *Adv. Mater.* **25**(18), 2517–2534 (2013).
26. B. Frank, X. Yin, M. Schäferling, J. Zhao, S. M. Hein, P. V. Braun, and H. Giessen, "Large-area 3D chiral plasmonic structures," *ACS Nano* **7**(7), 6321–6329 (2013).
27. T. J. Davis and E. Hendry, "Superchiral electromagnetic fields created by surface plasmons in nonchiral metallic nanostructures," *Phys. Rev. B* **87**(8), 085405 (2013).
28. A. García-Etxarri and J. A. Dionne, "Surface-enhanced circular dichroism spectroscopy mediated by nonchiral nanoantennas," *Phys. Rev. B* **87**(23), 235409 (2013).
29. D. Axelrod, T. P. Burghardt, and N. L. Thompson, "Total internal reflection fluorescence," *Annu. Rev. Biophys. Bioeng.* **13**(1), 247–268 (1984).
30. M. Tokunaga, K. Kitamura, K. Saito, A. H. Iwane, and T. Yanagida, "Single molecule imaging of fluorophores and enzymatic reactions achieved by objective-type total internal reflection fluorescence microscopy," *Biochem. Biophys. Res. Commun.* **235**(1), 47–53 (1997).
31. D. Axelrod, E. H. Hellen, and R. M. Fulbright, in *Topics in Fluorescence Spectroscopy: Biochemical Applications*, J. R. Lakowicz, ed. (Kluwer Academic, 2002).
32. H.-F. Fan, F. P. Li, R. N. Zare, and K.-C. Lin, "Characterization of two types of silanol groups on fused-silica surfaces using evanescent-wave cavity ring-down spectroscopy," *Anal. Chem.* **79**(10), 3654–3661 (2007).
33. P. B. Johnson and R. W. Christy, "Optical constants of the noble metals," *Phys. Rev. B* **6**(12), 4370–4379 (1972).
34. J. Dorfmueller, R. Vogelgesang, W. Khunsin, C. Rockstuhl, C. Etrich, and K. Kern, "Plasmonic nanowire antennas: experiment, simulation, and theory," *Nano Lett.* **10**(9), 3596–3603 (2010).
35. D. W. Pohl, S. G. Rodrigo, and L. Novotny, "Stacked optical antennas," *Appl. Phys. Lett.* **98**(2), 023111 (2011).
36. C.-H. Liu, C.-H. Chen, S.-Y. Chen, Y.-T. Yen, W.-C. Kuo, Y.-K. Liao, J.-Y. Juang, H.-C. Kuo, C.-H. Lai, L.-J. Chen, and Y.-L. Chueh, "Large scale single-crystal Cu(In,Ga)Se<sub>2</sub> nanotip arrays for high efficiency solar cell," *Nano Lett.* **11**(10), 4443–4448 (2011).
37. G. London, G. T. Carroll, T. Fernández Landaluce, M. M. Pollard, P. Rudolf, and B. L. Feringa, "Light-driven altitudinal molecular motors on surfaces," *Chem. Commun. (Camb.)* **2009**(13), 1712–1714 (2009).
38. N. P. M. Huck, W. F. Jager, B. de Lange, and B. L. Feringa, "Dynamic control and amplification of molecular chirality by circular polarized light," *Science* **273**(5282), 1686–1688 (1996).
39. J. J. D. de Jong, L. N. Lucas, R. M. Kellogg, J. H. van Esch, and B. L. Feringa, "Reversible optical transcription of supramolecular chirality into molecular chirality," *Science* **304**(5668), 278–281 (2004).
40. Y. Inoue, "Asymmetric photochemical reactions in solution," *Chem. Rev.* **92**(5), 741–770 (1992).
41. K. Ohkubo, T. Hamada, and M. Watanabe, "Novel photoinduced asymmetric synthesis of  $\Lambda$ -[Co(acac)<sub>3</sub>] from Co(acac)<sub>3</sub>(H<sub>2</sub>O)<sub>2</sub> and Hacac catalysed by racemic complexes of  $\Delta$ - and  $\Lambda$ -[Ru(menbpy)<sub>3</sub>]<sup>2+</sup> {menbpy = 4,4'-Di-[(1*R*,2*S*,5*R*)-(-)-menthoxycarbonyl]-2,2'-bipyridine; Hacac = pentane-2,4-dione}," *Chem. Commun.* **1993**(13), 1070–1072 (1993).

## 1. Introduction

Interaction between circularly polarized light (CPL) and chiral matter is of interest because it reveals structural details of molecules that can be critical for their chemical functions [1]. However, such interaction is usually weak due to the mismatch between pitch length of CPL and electronic confinement of the chiral matter [2, 3]. One example is the weak circular dichroism (CD) of chiral molecules. CD is the difference in absorption of left- and right-handed circularly polarized light (CPL) by a specific enantiomer of chiral matter. CD

originates from the coupling between induced electric dipole moment ( $\tilde{p}$ ) and magnetic dipole moment ( $\tilde{m}$ ) [4]. These quantities can be expressed as

$$\tilde{p} = \tilde{\alpha}\tilde{E} - i\tilde{G}\tilde{B}, \quad \tilde{m} = \tilde{\chi}\tilde{B} + i\tilde{G}\tilde{E}. \quad (1)$$

Here  $\tilde{\alpha}$  is the complex electric polarizability,  $\tilde{\chi}$  is the complex magnetic susceptibility,  $\tilde{G}$  is the isotropic mixed electric-magnetic dipole polarizability, and  $\tilde{E}$  and  $\tilde{B}$  are the complex electric and magnetic field. The absorption of light can be described by

$$\begin{aligned} A &= \langle E \cdot \dot{p} + B \cdot \dot{m} \rangle = \frac{\omega}{2} \text{Im}(\tilde{E}^* \cdot \tilde{p} + \tilde{B}^* \cdot \tilde{m}) \\ &= \frac{\omega}{2} \text{Im} \left\{ \tilde{\alpha} |\tilde{E}|^2 + \tilde{\chi} |\tilde{B}|^2 + i\tilde{G} (\tilde{E} \cdot \tilde{B}^* - \tilde{E}^* \cdot \tilde{B}) \right\}. \end{aligned} \quad (2)$$

Upon illumination of a time-harmonic electromagnetic field, whose complex electric and magnetic field can be expressed as  $\tilde{E} = (E_1 + iE_2)e^{-i\omega t}$  and  $\tilde{B} = (B_1 + iB_2)e^{-i\omega t}$ , respectively, Eq. (2) becomes

$$\begin{aligned} A &= \frac{\omega}{2} \text{Im} \left\{ \tilde{\alpha} |\tilde{E}|^2 + \tilde{\chi} |\tilde{B}|^2 + i\tilde{G} [-2i(E_1 \cdot B_2 - E_2 \cdot B_1)] \right\} \\ &= \frac{\omega}{2} (\alpha'' |\tilde{E}|^2 + \chi'' |\tilde{B}|^2) + \omega G'' \text{Im} \{ \tilde{E}^* \cdot \tilde{B} \}. \end{aligned} \quad (3)$$

Under illumination with moderate field intensity, the contribution from magnetic susceptibility  $\tilde{\chi}$  of most molecules can be safely neglected and Eq. (3) can be further simplified to

$$A^\pm = \frac{\omega}{2} \alpha'' |\tilde{E}|^2 \pm \omega G'' \text{Im} \{ \tilde{E}^* \cdot \tilde{B} \}, \quad (4)$$

where the superscript of  $A$  denotes different enantiomers with opposite sign of  $\tilde{G}$ . Therefore, the key to an enhanced CD is to obtain strongly enhanced electric fields that are parallel to the magnetic field with a phase difference of  $\pi/2$  [5–7].

Recently, CD is linked to the “optical chirality” proposed by Lipkin in 1964 [8, 9]. The optical chirality “ $C$ ” of an electromagnetic field was defined by Lipkin as

$$C \equiv \frac{\epsilon_0}{2} E \cdot \nabla \times E + \frac{1}{2\mu_0} B \cdot \nabla \times B = -\frac{\epsilon_0}{2} \omega \text{Im} \{ \tilde{E}^* \cdot \tilde{B} \}, \quad (5)$$

where  $\epsilon_0$  and  $\mu_0$  are the permittivity and permeability of free space, respectively. Using optical chirality, Eq. (4) becomes

$$A^\pm = \frac{2}{\epsilon_0} (\omega U_e \alpha'' \mp CG''), \quad (6)$$

where  $U_e = \frac{\epsilon_0}{4} |\tilde{E}|^2$  is the time-average energy density of the electric field. Note that the physical meaning of the first term is the conventional dipolar absorption and the true origin of CD is the second term. In other words, to truly enhance the absorption difference, one needs to engineer the field such that the optical chirality is maximized.

To report CD effect, a commonly used quantity is the dissymmetry factor “ $g$ ” defined as

$$g \equiv \frac{2(A^+ - A^-)}{(A^+ + A^-)}. \quad (7)$$

Inserting Eq. (6) into Eq. (7), the dissymmetry factor can be expressed as

$$g = -\left(\frac{G''}{\alpha''}\right)\left(\frac{2C}{\omega U_e}\right). \quad (8)$$

By minimizing the  $U_e$ , Cohen and associates showed enhanced contrast in fluorescence-detected circular dichroism (FDCD) of chiral molecules at energy minima of a standing CPL wave [10]. However, the minimum energy density also means minimum excitation rate and thus minimum fluorescence intensity, which limits the detection sensitivity. In fact, the  $U_e$  in the denominator of Eq. (8) stems from the fact that the dissymmetry factor is a “normalized” quantity that takes the ratio of CD to conventional dipolar absorption. Such normalization is, however, not always necessary. For example, ellipticity of CPL after passing through chiral material is solely a function of the difference in absorption [4]. The ellipticity reads  $[\theta] = 3300(\varepsilon_+ - \varepsilon_-) = 3300\Delta\varepsilon$ , where  $\varepsilon$  is the absorbance of the enantiomers. In this case, the CD is directly reported as a function of the differential absorption of CPL. In other words, increasing optical chirality is the key to truly enhance CD, whereas decreasing the averaged energy density is just to enlarge the typically small dissymmetry factor without enhancing the absorption difference.

Resonant plasmonic nanostructures can localize and enhance optical near field. Therefore, they may function as optical antennas and improve the mismatch between light and nanoscale objects [11–13]. The ability of plasmonic nanostructures to enhance and sculpt optical near fields has recently drawn research attention. On the one hand, various plasmonic nanostructures have been proposed to manipulate the polarization state of light field or to show chiroptical response themselves [14–26]. On the other hand, plasmonic nanostructures and dielectric particles have been reported to create light fields for enhancing chiral light-matter interaction [5–7, 27, 28].

Here, we present a new design of slant-gap plasmonic nanoantennas and theoretically show that optical chirality of the field in the slant gap is greatly enhanced upon resonant excitation. The working principle is based on the fact that the electric field lines at the vicinity of nanostructures are well perpendicular to the metal boundaries. Therefore, the optical near field in the slant gap automatically provides a component perpendicular to the longitudinal axis of antenna. At longitudinal resonance of the antenna, such electric field component is greatly enhanced in amplitude, delayed  $\pi/2$  in phase and well parallel to the magnetic field of external excitation. As a result, an enhanced optical chirality is obtained inside the gap. We choose to excite the slant-gap nanoantenna with the near field of linearly polarized plane wave undergoing total internal reflection (TIR). Such TIR excitation scheme can efficiently suppress the background and is particularly useful for CD analysis of ultra-dilute chiral matter at surface [29–32].

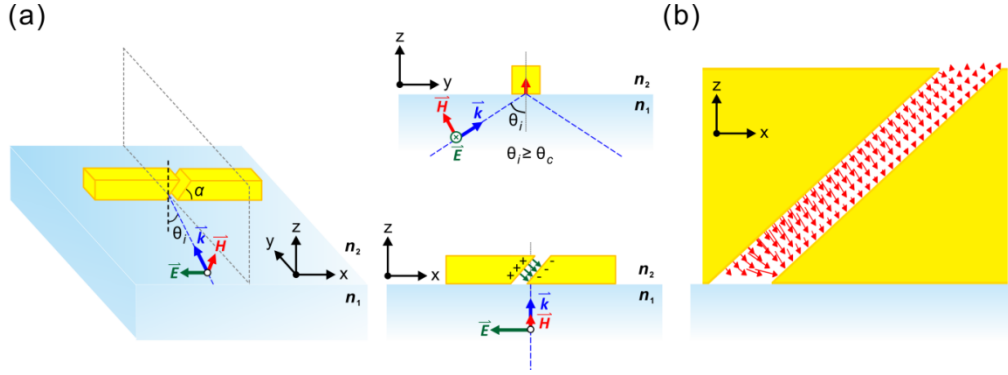


Fig. 1. (a) Schematic diagrams of a slant-gap plasmonic nanoantenna illuminated with the near field of s-polarized plane waves undergoing total internal reflection.  $\alpha$  is the slant angle and  $\theta_i$  is the impinging angle of the plane wave and is larger than the critical angle  $\theta_c$  for total internal reflection.  $n_1$  and  $n_2$  are the refractive index of the glass substrate and air, respectively. The electric field  $\vec{E}$ , magnetic field  $\vec{H}$  and the wavevector  $\vec{k}$  are indicated with green, red and blue arrows, respectively. (b) The stimulated electric field lines (red arrows) in the slant gap are well perpendicular to the metal boundaries.

## 2. x-z slant antennas + TE-TIR

Figure 1(a) shows the design of the slant-gap plasmonic nanoantenna. The gold nanoantenna has a square cross section ( $30 \times 30 \text{ nm}^2$ ) and a slant gap (separation in x-direction = 10 nm) tilted in x-z plane by  $\alpha$  degree with respect to the surface, *i.e.* the x-y plane. The excitation source is s-polarized plane wave undergoing TIR at air/glass interface on x-y plane. For the excitation configuration in Fig. 1(a), the significant near-field components at the TIR interface are

$$\vec{E}_x = \left[ \frac{2 \cos \theta}{(1 - n^2)^{1/2}} \right] A_s e^{-i\delta_s}, \quad (9)$$

$$\vec{H}_y = \left[ \frac{2 \cos \theta (\sin^2 \theta - n^2)^{1/2}}{(1 - n^2)^{1/2}} \right] A_s e^{-i(\delta_s - \pi)}, \quad (10)$$

and

$$\vec{H}_z = \left[ \frac{2 \cos \theta \sin \theta}{(1 - n^2)^{1/2}} \right] A_s e^{-i\delta_s}, \quad (11)$$

where  $\delta_s = \tan^{-1} \left[ \frac{(\sin^2 \theta - n^2)^{1/2}}{\cos \theta} \right]$ ,  $\theta$  is the TIR incident angle,  $n = n_2/n_1 < 1$  and  $A_s$  is the amplitude of s-polarized electric field component of the impinging plane waves [29, 31]. For a nanoantenna on the interface and aligned in x direction, the  $\vec{E}_x$  component of the TIR near field excites the longitudinal surface plasmon resonance and results in highly enhanced optical near field with certain phase shift inside the gap [13]. The field in the gap,  $\vec{E}_g$  can be expressed as

$$\bar{E}_g = f_e |\bar{E}_x| e^{-i\varphi_r} \cdot \hat{n}, \quad (12)$$

where  $\bar{E}_x$  is the longitudinal electric field component of the TIR near field at the interface,  $\varphi_r$  is the phase delay relative to external excitation,  $f_e$  is the field amplitude enhancement and  $\hat{n}$  is the unit vector normal to the metal surface. At resonance, the phase shift approaches 90 degree and the field enhancement reaches a maximum value. Since the gap is slant, the enhanced field in the gap is no longer parallel to the antenna long axis, as shown in Fig. 1(b). As a result, the resonant optical near field automatically provides an out-of-plane electric field component  $\bar{E}_z$ , which can be expressed as

$$\bar{E}_z = \bar{E}_g \cdot \cos \alpha, \quad (13)$$

with  $\alpha$  being the slant angle of the gap relative to the interface (x-y plane). Such an out-of-plane electric field component is parallel to the out-of-plane magnetic field components of the TIR near field ( $\bar{H}_z$ ), leading to an enhanced optical chirality in the gap. Combining Eq. (5), (9), (11), (12) and (13), the optical chirality can be expressed as

$$C = - \left[ \frac{2\varepsilon_0 \omega \cos^2 \theta \sin \theta}{(1-n^2)} \right] A_x^2 f_e \cos \alpha \sin \varphi_r. \quad (14)$$

For constant  $n$ ,  $\theta$  and  $\omega$ , optical chirality of the near field in the gap is a function of  $f_e$ ,  $\varphi_r$  and  $\alpha$ . In the following, we numerically study the optical chirality in the gap as a function of antenna resonance condition and the slant angle of the gap.

All the simulations in this work are performed using the finite-difference time-domain method (FDTD Solutions v8.6.4, Lumerical Solutions, Inc.). The permittivity of Au is taken from experimental data [33], and the refractive index of glass is set to be a constant at  $n = 1.45$ . The mesh size is  $2 \times 2 \times 2 \text{ nm}^3$  for the whole slant-gap nanoantenna and an additional mesh override area with mesh size of  $1 \times 1 \times 1 \text{ nm}^3$  is used for the gap region. Note that total electric and magnetic fields are obtained from FDTD simulations, meaning that the effect of interference between incident and induced fields has been taken into consideration. In order to evaluate the enhancement effect, we calculate the optical chirality enhancement (OCE) by normalizing the optical chirality at every point in space to the absolute optical chirality of circularly polarized plane wave of the same power propagating in vacuum.

$$OCE_{x,y,z} = \frac{-\frac{\varepsilon_0}{2} \omega \text{Im} \{ \tilde{E}_{x,y,z}^* \cdot \tilde{B}_{x,y,z} \}}{\left| -\frac{\varepsilon_0}{2} \omega \text{Im} \{ \tilde{E}_0^* \cdot \tilde{B}_0 \} \right|} = \frac{C_{x,y,z}}{|C_0|}. \quad (15)$$

Here,  $C_0$  denotes the absolute optical chirality of circularly polarized plane wave propagating in vacuum. To estimate the total effect of one single nanoantenna in enhancing CD of randomly distributed chiral matter, we further calculate the overall OCE by integrating OCE over the open space around the antenna.

$$\text{Overall OCE} = \iiint OCE_{x,y,z} dx dy dz. \quad (16)$$

Since the near field decays exponentially from the metal surface, we only integrate OCE within a minimum but representative area. The distance from the antenna surface to the boundaries of the integration box is set to be a constant  $d$ , as shown in Fig. 2(a). We exclude the space inside the antenna arms and glass substrate because they are not accessible to chiral

matter. Figure 2(b) shows the overall OCE as a function of  $d$  for the 160-nm antenna at the fundamental resonance. It can be seen that the overall OCE saturates at  $d = 10$  nm. Therefore, we have chosen  $d = 10$  nm for our overall OCE calculation. Although the antenna corners also show OCE, the sign alternates and the contribution vanishes when OCE is integrated over space [6]. Therefore, the overall OCE is dominated by the field inside the gap.

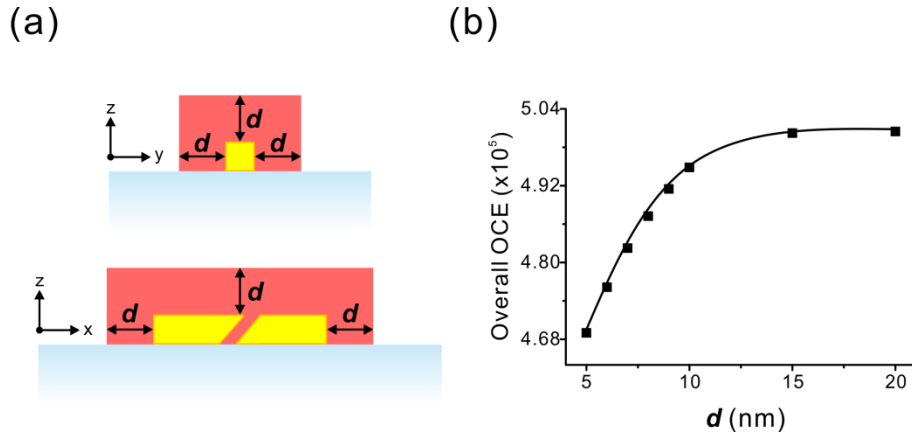


Fig. 2. (a) The integration area (in red color) for the calculation of overall OCE. The glass half space and the area inside the antenna arms are excluded since they are not accessible to chiral matter. (b) Overall OCE value as a function of  $d$  for the 160-nm antenna at the fundamental resonance. Solid line is a guide line for the eye.

### 3. The effect of the total antenna length

Figure 3(a) shows the intensity enhancement and the phase shift of the field inside the gap as a function of the total antenna length. For a fixed excitation frequency at 374 THz (wavelength in vacuum = 800 nm), a total antenna length of 160 nm hits the fundamental resonance and leads to the first maximum of field intensity enhancement. The phase shift is +90 degree with respect to the external excitation field. As the antenna length further increases, higher order resonances gradually emerge [34]. The first higher order resonance appears around antenna length of 480 nm with a phase shift of -90 degree. Compared to the fundamental resonance, the first higher order resonance exhibits lower intensity enhancement and possesses opposite phase shift. This has a direct consequence on the sign and magnitude of the optical chirality of the field in the gap.

The overall OCE as a function of antenna length (Fig. 3(b)) reaches a maximum value when the antenna length is at the fundamental resonance. Considering Eq. (5), it is clear that the maximum OCE value is a direct result of simultaneous fulfillment of maximum electric field and 90 degree phase shift between parallel electric and magnetic field at the fundamental antenna resonance. For antenna lengths that are out of resonance, the overall OCE value quickly drops to zero. As the antenna length hits the first higher order resonance, the overall OCE switches its sign and reaches a local minimum, *i.e.* a most negative OCE. The absolute OCE value for the higher order resonance is smaller since the field enhancement factor  $f_e$  is smaller due to larger plasmon damping on longer antenna arms. As for the opposite sign, it stems from the opposite resonance phase  $\varphi_r$  for the first higher order resonance. The phase difference between fundamental and the first higher order resonance is a result of different current distribution in the antenna arms. Figure 3(c) shows the real part of displacement current ( $\text{Re}\{J_x\}$ ) and the out-of-plane electric field component ( $\text{Re}\{\vec{E}_z\}$ ), as well as the OCE distribution of the two resonance conditions on the x-z plane cutting through the antenna center. It can be seen that the current distribution on the antenna arms has opposite sign near

the gap for the two resonances. This leads to opposite  $\text{Re}\{\bar{E}_z\}$  in the gap and therefore opposite sign of OCE in the gap.

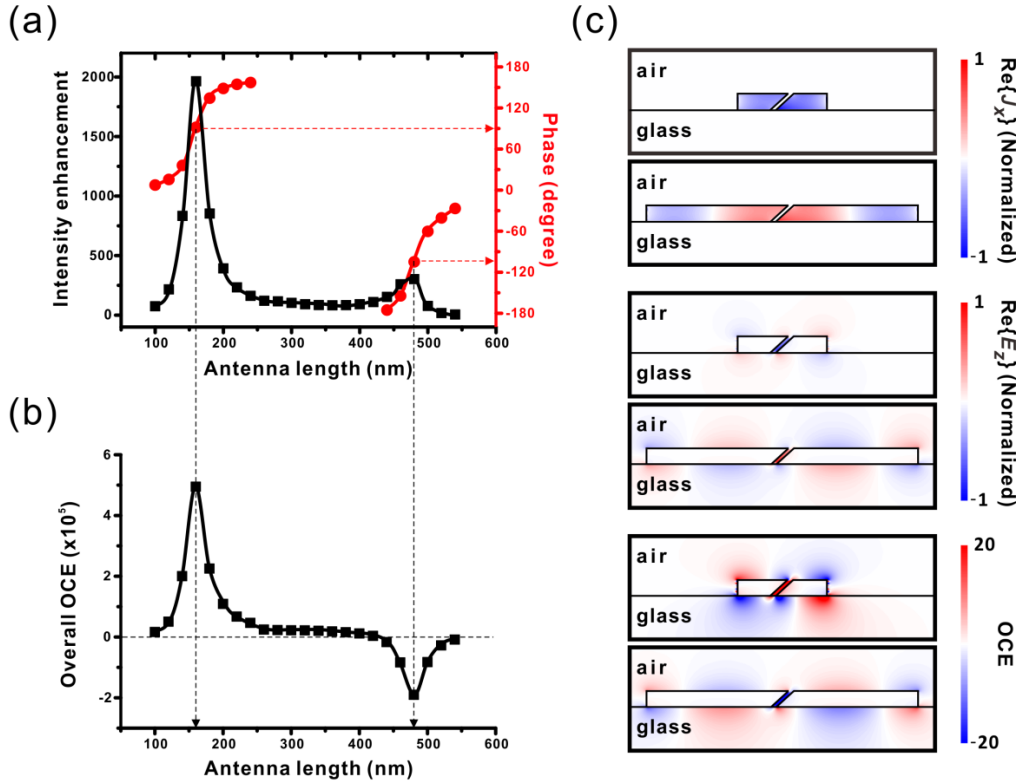


Fig. 3. (a) Intensity enhancement (black squares) and the spectral phase (red dots) of the field in the slant gap as functions of the total antenna length. (b) Overall optical chirality enhancement (OCE) as a function of antenna length. (c) Distribution of displacement current (top panel), out-of-plane electric-field component ( $\bar{E}_z$ , middle panel) and OCE (bottom panel) of the antenna at fundamental resonance (total length = 160 nm) and the first higher order resonance (total length = 480 nm).

#### 4. The effect of the slant angle

Since the magnitude of out-of-plane electric field is proportional to  $\cos\alpha$ , it is intuitive to choose a small  $\alpha$  in order to obtain large OCE. However, varying slant angle can change the antenna geometry significantly and distort the resonance spectrum. Consequently, the field enhancement factor ( $f_e$ ) varies with the slant angle. Therefore, the slant angle must be optimized carefully such that  $f_e \times \cos\alpha$  is maximized. Figure 4(a) shows the resonance frequency and the field amplitude enhancement  $f_e$  (for 160-nm antenna at 374 THz) as functions of the slant angle. Both quantities vary with the slant angle and the field enhancement  $f_e$  reaches the maxima when the resonance frequency matches the desired frequency. As shown in Fig. 4(b), increasing the slant angle from 15 to 165 degree, the overall OCE exhibits extreme values with opposite sign at  $\alpha = 45$  and  $\alpha = 135$  degree and crosses zero value at  $\alpha = 90$  degree. The trend of overall OCE obtained from 3-dimensional full-wave FDTD simulations well follows the trend of  $f_e \times \cos\alpha$ , as shown by the blue dashed line in Fig. 4(b). Figure 4(c) shows the OCE distribution for  $\alpha = 45, 90$  and  $135$  degree.

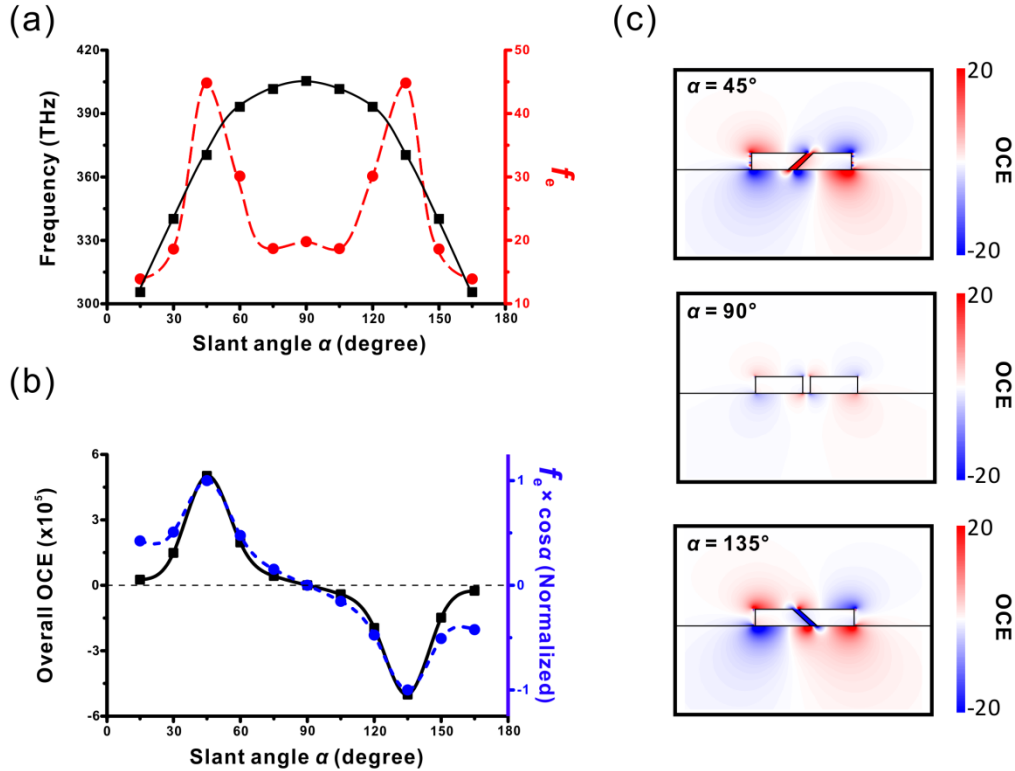


Fig. 4. (a) Resonant frequency (squares, black solid line) and the field enhancement (dots, red dashed line) as functions of the slant angle of the gap. (b) Overall optical chirality enhancement (OCE, squares, black solid line) and the product of  $f_e \times \cos\alpha$  (dots, blue dashed line) as functions of the slant angle of the gap. (c) The cross sectional OCE distributions of various slant angle.

It is worth noting that while the sign of OCE in the gap changes with the slant angle, the OCE patterns at antenna outer corners remain the same regardless of the sign of slant slope. This suggests that the field in the gap dominates the overall OCE and the OCE at outer corners vanishes in the integration. In practical applications, changing the sign of the slant slope can be easily achieved by changing the impinging direction of the plane wave in TIR scheme, instead of fabricating new structures. Using the previously proposed stacked antenna [35] may also lead to resonance-enhanced optical chirality in the gap. However, the stacked gap is not open to chiral matter and periodic stacked structures, if possible, would result in cancellation of optical chirality.

## 5. Other configurations

In addition to the configurations discussed above, there are other possible excitation geometries, as shown in Fig. 5. The field enhancement at the gap center and the overall OCE of the slant-gap antenna at fundamental resonance (antenna length = 160 nm, slant angle = 45 degree) under these illumination geometries are summarized in Table 1. These geometries show either very small or zero overall OCE. For example, normally incident excitation (Fig. 5(a)) gives large field enhancement in the gap but results in zero overall OCE because the enhanced electric fields are orthogonal to the magnetic field. As for the excitation geometry shown in Fig. 5(b), it is similar to the geometry in Fig. 1(a) but using p-polarized incident plane waves.

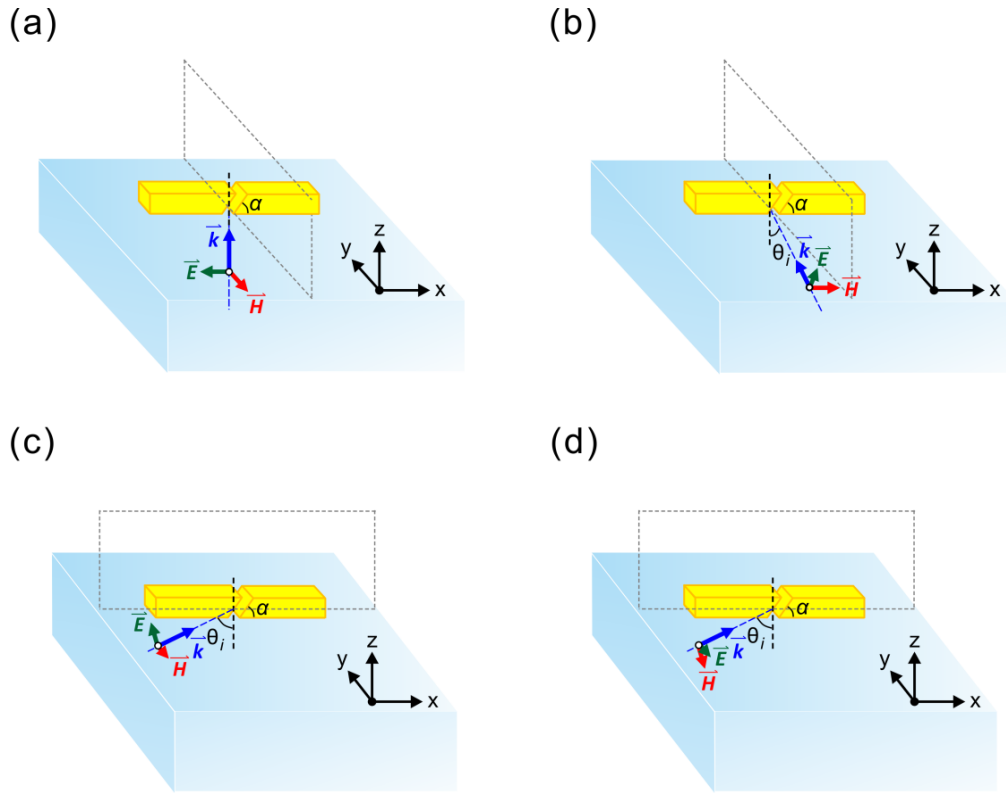


Fig. 5. Schematic diagram of different excitation configurations, including (a) normally incident excitation linearly polarized in longitudinal antenna axis, (b) p-polarized TIR excitation with magnetic field parallel to the longitudinal axis of antenna, (c) p-polarized TIR excitation with magnetic field perpendicular to the longitudinal axis of antenna and (d) s-polarized TIR excitation with electric field component perpendicular to the longitudinal axis of antenna.

Finite OCE is obtained due to the overlap of in-plane electric ( $\bar{E}_x$ ) and magnetic field component ( $\bar{H}_x$ ). However, the OCE is much smaller since it relies on the transverse resonance of the antenna that has relatively low field enhancement at 374 THz. In fact, the slant gap concept is general and the slant angle is not limited to out-of-plane direction (*i.e.* x-z plane in Fig. 1). The gap may also be tilted in-plane (*i.e.* x-y plane in Fig. 1), as long as the excitation geometry is adjusted accordingly.

**Table 1. Gap field enhancement and overall optical chirality enhancement (OCE) of various excitation configurations shown in this work.**

Configuration	Field enhancement ( $f_e$ )	Overall OCE
Figure 5(a)	60.36	0
Figure 5(b)	2.79	21360
Figure 5(c)	28.56	0
Figure 5(d)	0.17	0
Figure 1(a)	44.32	494852

## 6. Extended structures: slant grooves

In order to maximize the interaction area, the slant-gap concept can be extended into an array of grooves, as depicted in Fig. 6(a). The lateral cross section in x-z plane is essentially an

array of antenna arms. Similar to solitary gap nanoantennas, the resonance can be tuned by changing the material, the thickness, the gap size and the periodicity. Figures 6(b) and 6(c) show the cross sectional distribution of OCE in x-z plane and x-y plane, respectively. The period of the gold slant groove array is 100 nm. The height and the gap size are 30 nm and 10 nm, respectively. Compared to solitary antennas, the resonance condition changes and the field enhancement decreases due to the inter-arm coupling and the extended dimension in y direction. Nevertheless, the OCE inside the gap has a non-zero value with a sign that is slant angle dependent. The overall OCE obtained from integration over the cross sectional area of a unit cell also shows finite non-zero value that is dominated by the field in the gap. The OCE at outer corners exhibits alternating sign and do not contribute to overall OCE. In practice, depositing a layer of transparent dielectric material may further prevent the chiral matter from interaction with the corner fields. Slant groove array can be easily fabricated by modern nanofabrication techniques, for example by focused-ion beam (FIB) milling with a tilted angle. Figure 6(d) shows a representative example of an array of slant grooves on a single crystalline gold flake fabricated by FIB milling with a tilt angle of 52 degree relative to the sample surface normal. Other lithography methods such as e-beam lithography might also be applied to fabricate slant grooves by, for example, tilting the sample during the evaporation or dry etching [36].

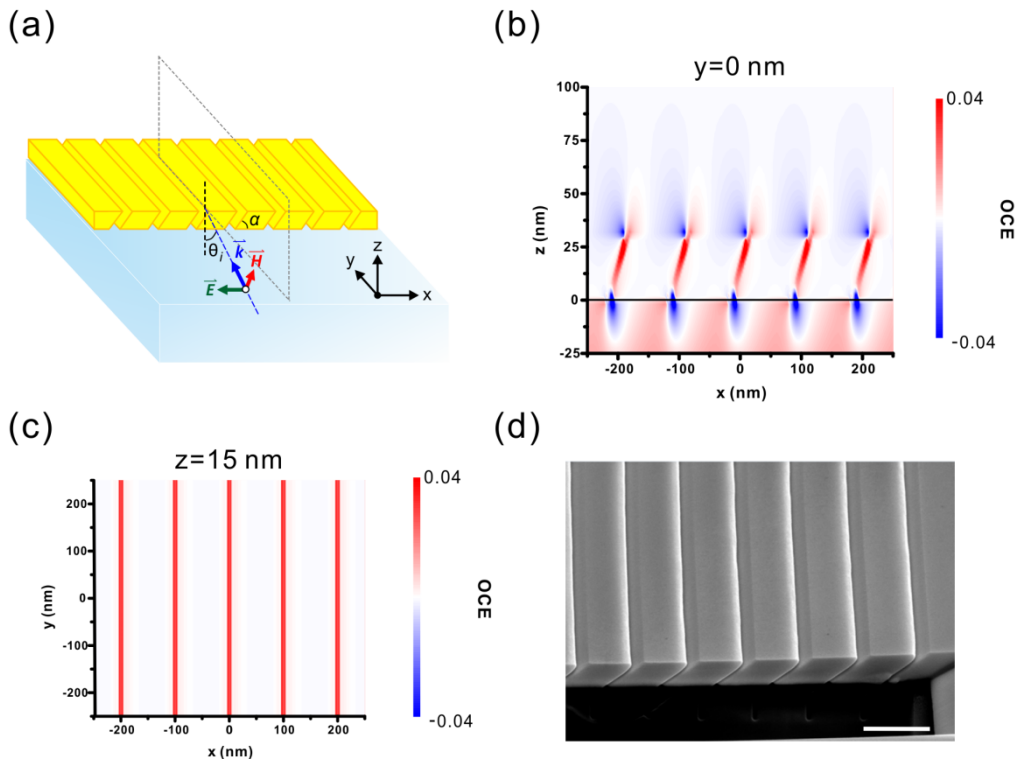


Fig. 6. (a) Schematic diagram of slant plasmonic grooves illuminated by the near field of s-polarized plane wave undergoing total internal reflection (TIR). The thickness of the gold film is 30 nm and the gap separation in x-direction is 10 nm.  $\theta_i$  is the incident angle of the TIR excitation and  $\alpha$  is the slant angle of the gap with respect to the surface plane. (b) Cross sectional OCE distribution in x-z plane. (c) OCE distribution in x-y plane cutting through the middle height of the gold film. (d) Representative SEM image of the slant groove array on a single crystalline gold flake. Scale bar is one micrometer.

## 7. Conclusion

We have presented the design of slant-gap nanoantennas excited by total internal reflection scheme. The slant gap offers strong field with enhanced optical chirality that can be controlled and optimized by the resonance condition and the slant angle of the gap. Our slant-gap nanoantenna enables CD analysis with linearly polarized light. This facilitates the CD analysis of chiral matter at the surface [37]. The use of total internal reflection scheme also minimizes the background. The enhanced difference in absorption may also facilitate photo-induced chirality control [38, 39] and asymmetry chemical synthesis [40, 41]. Our design is simple and easy to realize. We anticipate many applications in plasmon-enhanced chirality detection and control.

## Acknowledgments

Supports from National Science Council of Taiwan under Contract Nos. NSC-99-2113-M-007-020-MY2 and NSC-101-2113-M-007-002-MY2 are gratefully acknowledged. JSH thanks the support from Center for Nanotechnology, Materials Science, and Microsystems at National Tsing Hua University.